Porous Iron Molybdate Nanorods: In situ Diffusion Synthesis and Low-Temperature H$_2$S Gas Sensing

Yu-Jin Chen,*,[†] Xin-Ming Gao,[†] Xin-Peng Di,[†] Qiu-Yun Ouyang,[†] Peng Gao,*,[‡] Li-Hong Qi,[†] Chun-Yan Li,[†] and Chun-Ling Zhu*,[‡]

[†]Key Laboratory of In-Fiber Integrated Optics of Ministry of Education, College of Science, and [‡]College of Material Science and Chemical Engineering, Harbin Engineering University

Ⓢ *Supporting Information*

ABSTRACT: In the paper, we developed an in situ diffusion growth method to fabricate porous Fe$_2$(MoO$_4$)$_3$ nanorods. The average diameter and the length of the porous nanorods were 200 nm and 1.2−4 μm, respectively. Moreover, many micropores existed along axial direction of the Fe$_2$(MoO$_4$)$_3$ nanorods. In terms of nitrogen adsorption−desorption isotherms, calculated pore size was in the range of 4−115 nm, agreeing well with the transmission electron microscope observations. Because of the uniquely porous characteristics and catalytic ability at low temperatures, the porous Fe$_2$(MoO$_4$)$_3$ nanorods exhibited very good H$_2$S sensing properties, including high sensitivity at a low working temperature (80 °C), relatively fast response and recovery times, good selectivity, and long-term stability. Thus, the porous Fe$_2$(MoO$_4$)$_3$ nanorods are very promising for the fabrication of high-performance H$_2$S gas sensors. Furthermore, the strategy presented here could be expended as a general method to synthesize other hollow/porous-type transition metal molybdate nanostructures by rational designation in nanoscale.

Fe(OH)$_3$@α-MoO$_3$ nanostructures → Porous Fe$_2$(MoO$_4$)$_3$ nanorods

KEYWORDS: *Iron molybdate, porous nanostructure, diffusion growth, gas sensor, low-temperature sensing*
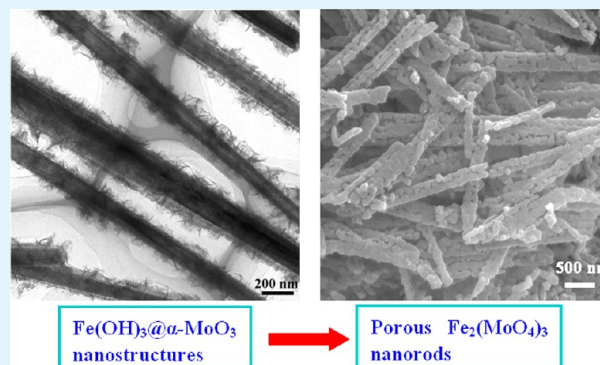
1. INTRODUCTION

Iron molybdate (Fe$_2$(MoO$_4$)$_3$), as an important functional material, has been demonstrated to possess properties useful for applications in gas sensing, methanol and propene oxidation, and magnetic devices.[1−18] Therefore, in the past few years, several approaches including solid-state reactions, coprecipitation, and sol−gel methods have been developed to fabricate Fe$_2$(MoO$_4$)$_3$ powder. Much work before mainly focused on the control of the Mo/Fe ratio because it has important effect on the catalytic activity of Fe$_2$(MoO$_4$)$_3$; however, to the best of our knowledge, the control of the morphology of the material is rarely reported.[19−21] Among various morphologies, the porous or hollow nanostructures may exhibit better physicochemical properties because of their higher surface areas. So far, the most common method to fabricate porous or hollow nanostructures involves the use of templates such as carbonaceous and polystyrene spheres, and silica materials.[22−26] However, the successful synthesis of the porous or hollow nanostructures need carefully eliminate the templates form composite nanostructures, leading to a very complex and time-consuming process. Recently, template-free strategy based on the Kirkendall effect or Ostwald ripening mechanism has attracted much attention for the synthesis of porous or hollow nanostructures because of simple processes.[27−35] Many porous or hollow nanostructures, including α-Fe$_2$O$_3$ nanotubes, Cu$_2$O nanocages and hollow nanospheres, porous SnO$_2$ nanostructures, hollow Fe$_2$O$_3$/SnO$_2$ core/shell nanostructures, α-Fe$_2$O$_3$/TiO$_2$ tubelike nanostructures, porous carbon/Fe$_3$O$_4$ nanorods, have been synthesized.[27−35] Despite these two useful strategies, the synthesis of porous ternary metal oxide nanostructures still remains a challenge. Recently, molybdate structures were successfully fabricated by a simple hydrothermal method.[36−39] Specially, the successful fabrication of one-dimensional (1D) nanostructured metal molybdate hydrates or metal molybdate extended the application areas of these materials, i.e., in photoelectric devices. However, up to now, the synthesis of 1D porous metal molybdate nanostructures has seldom been reported.[19]

Increased concerns with the toxic effects of chemicals on the environment lead to rapid development of gas sensors for monitoring of pollutions. According to the safety standards established by American Conference of Government Industrial Hygienists, the threshold limit value defined for H$_2$S is 10 ppm. As the H$_2$S concentration is higher than 250 ppm, it is very dangerous to the human body. Therefore, it is necessary to explore fast-response sensors to detect trace H$_2$S gas in the environment. Recently, gas sensors based on metal oxide semiconductors have attracted much attention because of their rich sources, low cost, and facile fabrication. Among them, semiconductors such as SnO$_2$, ZnO, WO$_3$, and In$_2$O$_3$ nanostructures

can be successfully used for the detection of ethanol at ppm level.[40−42] However, they exhibited weak response to H_2S gas even at a high working temperature. Therefore, several methods such as catalyst functionalization, elemental doping, and heterostructure formation have been developed to improve the sensitivity of gas sensors.[43−50] Among these strategies, the construction of p−n junction heteronanostructures is considered as a very efficient approach to improve the sensitivity of the sensors. For example, the sensitivity of SnO_2/CuO core/shell nanorods was up to 9.4×10^6 to 10 ppm H_2S at a working

temperature of 60 °C. However, the response of the nanorods was not recovered at the low working temperature.[49]

Herein we develop an in situ diffusion growth method to fabricate porous $Fe_2(MoO_4)_3$ nanorods. On one hand, the in situ diffusion growth method is easily achieved with large-scale production of the nanorods because it only involves a simply stirring process and a subsequently heating treatment. On the other hand, with the core materials consumed, the micropores are produced in the final product, which significantly enhances the surface area of the product. Therefore, the porous $Fe_2(MoO_4)_3$ nanorods synthesized by the in situ growth method not only can detect 1 ppm H_2S gas at a low working temperature (80 °C), but also their recovery time is relatively fast. Moreover, the strategy presented here could be expended as a general method to synthesize other hollow/porous-type transition metal molybdate nanostructures by rational designation in nanoscale.
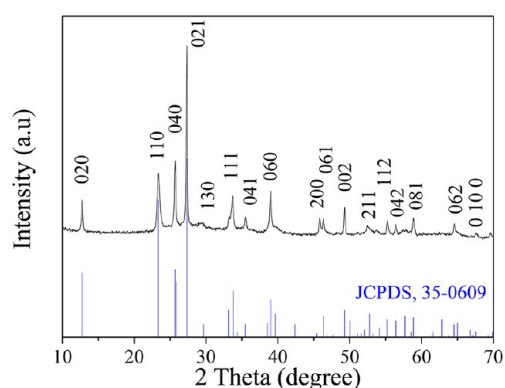
Figure 1. XRD pattern of the $Fe(OH)_3@\alpha\text{-}MoO_3$ core/shell nanostructures.

2. EXPERIMENTAL SECTION

2.1. Synthesis of $\alpha\text{-}MoO_3$ Nanorods. All of the reagents are analytically pure, were purchased and used without further purification. The $\alpha\text{-}MoO_3$ nanorods were first synthesized by a hydrothermal method described elsewhere.[45,51] Simply, 7.2 g of $\alpha\text{-}MoO_3$ powder was reacted with 55 mL of 30% aqueous H_2O_2 and dissolved completely under stirring. Twenty-seven mL of concentrated nitric acid and 170 mLof distilled water were added to the solution above, respectively. The mixture was allowed to stand for 4 days at room temperature. 35 mL of the mixture was then transferred into a Teflon-lined stainless steel autoclave with a capacity of 50 mL for hydrothermal treatment at 170 °C for 24 h.
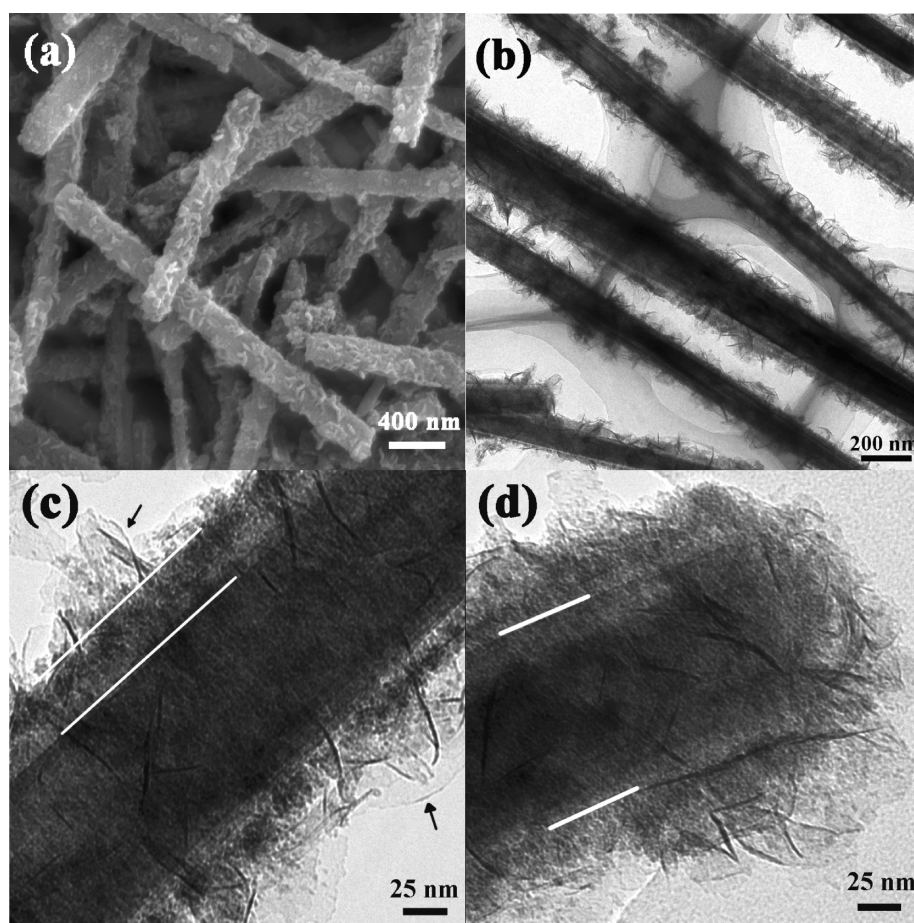
Figure 2. Structural characterization of the $Fe(OH)3@\alpha\text{-}MoO_3$ core/shell nanostructures. (a) SEM image, (b) low-resolution TEM image, (c, d) magnified TEM images. The $Fe(OH)_3$ thin film and nanoplates are marked the with white lines and the black arrows in Figure 2c, respectively. The $\alpha\text{-}MoO_3$ core is located at the region between the two white lines in d.

As the autoclave cooled to room temperature naturally, the precipitates were separated by centrifugation, washed with distilled water and absolute ethanol, and dried in air.

2.2. Synthesis of Fe(OH)$_3$@α-MoO$_3$ Core/Shell Nanorods. 0.075 g of α-MoO$_3$ nanorods were dispersed into 100 mL distilled water under vigorous stirring. 0.9 g of Fe(NO$_3$)$_3$·9H$_2$O was added into the suspension. The above mixture was kept at 50 °C for 2 h under stirring. The precipitate was separated by centrifugation, washed with distilled water and ethanol, and then dried in air. The obtained powder was treated in the Fe(NO$_3$)$_3$·9H$_2$O solution again through the same process above in order to allow more amount of Fe(OH)$_3$ to deposit on the surface of α-MoO$_3$ nanorods.

2.3. Synthesis of Porous Fe$_2$(MoO$_4$)$_3$ Nanorods. The dried Fe(OH)$_3$@α-MoO$_3$ nanorods were thermally treated at 500 °C for 4 h in air, and then the porous Fe$_2$(MoO$_4$)$_3$ nanorods were obtained.

2.4. Characterization. The morphology and size of the synthesized samples were characterized by scanning electron microscope (SEM) [HITACHI S−5200] and an FEI Tecnai-F20 transmission electron microscope (TEM) equipped with a Gatan imaging filter (GIF). The crystal structure of the sample was determined by X-ray diffraction (XRD) [D/max 2550 V, Cu Kα radiation]. X−ray photoelectron spectroscopy (XPS) measurements were carried out using a spectrometer with Al Kα radiation (PHI 5700ESCA System). The pore diameter distribution and surface area were tested by nitrogen adsorption/desorption analysis with a Quantachrome Instruments (Autosorb-iQ2-MP).

2.5. Sensor Fabrication and Sensing Measurements. The fabrication and testing principle of the gas sensor are similar to those described in our previous reports.[42,43] Briefly, the sensing materials were dispersed in ethanol, and ground in an agate mortar to form a paste. The paste was spun onto a ceramic tube between metal electrodes to form a thin film. A heating wire in the ceramic tube was used to control the working temperature of the sensor. The gas sensing properties were tested by ZWS1-WS-30A system (Zhongxiyuanda Science and Technology Co. Beijing, China), equipped with a chamber and 30 tested channels. Detected gases such as H$_2$S were injected into the test chamber and mixed with air. The sensor response to reductive gas was defined as $S = R_a/R_g$, where R_g is the resistance in target-air mixed gas and R_a is the sensor resistance in air, respectively.

3. RESULTS AND DISCUSSION

3.1. Growth of Fe(OH)$_3$@α-MoO$_3$ Nanostructures. It is well-known that amorphous Fe(OH)$_3$ colloid nanoparticles can be formed during the hydrolysis process of Fe(NO$_3$)$_3$·9H$_2$O even at room temperature.[21,52,53] Under the present experimental conditions (at 50 °C), the reaction, Fe^{3+} + 3H$_2$O → Fe(OH)$_3$ + 3H$^+$, occurs more easily. As the α-MoO$_3$ nanorods are added in the solution, the amorphous Fe(OH)$_3$ nanoparticles will preferentially deposit on the surface of the α-MoO$_3$ nanorods because they can be used as supported substrates. With the reaction time prolonged, the Fe(OH)$_3$@α-MoO$_3$ nanostructures will be formed.[21,52] As the Fe(OH)$_3$@α-MoO$_3$ nanostructures were treated in Fe(NO$_3$)$_3$ solution under the same conditions again, the previously deposited Fe(OH)$_3$ nanoparticles serves as "seeds" and promote their further growth, leading to the formation of the relatively complicated Fe(OH)$_3$@α-MoO$_3$ core−shell nanostructures.

Figure 1 shows a typical XRD pattern of the Fe(OH)$_3$@α-MoO$_3$ nanorods, in which the blue lines denote the location of the diffraction peaks of the orthorhombic α-MoO$_3$ (JCPDS, no. 35−0609, cell parameters: a = 3.963 Å, b = 13.856 Å, c = 3.6966 Å). All diffraction peaks marked with Miller indices in the pattern can be indexed to the α-MoO$_3$. No peaks from other materials were detected by the XRD measurement, suggesting that Fe(OH)$_3$ in the Fe(OH)$_3$@α-MoO$_3$ core/shell nanostructures is amorphous. The result is proved by the XPS measurement, as shown in Figure S1 (see the Supporting Information).
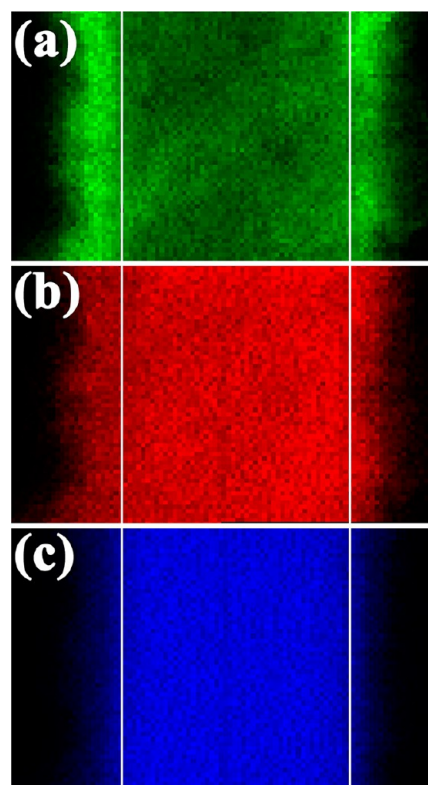

Figure 3. EDX elemental mappings of Fe(OH)$_3$@α-MoO$_3$ core/shell nanostructures. (a) Fe, (b) O, and (c) Mo elements. The area of the single nanorod is marked with the white lines in the figure.
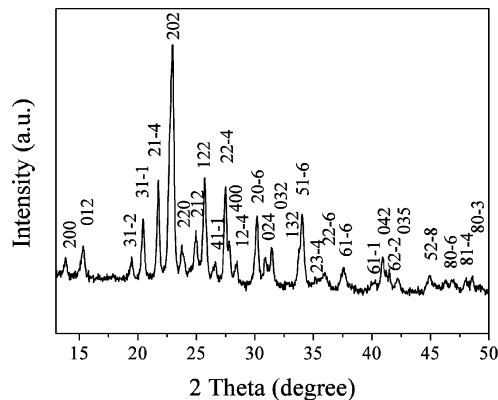
Figure 4. XRD pattern of the porous Fe$_2$(MoO$_4$)$_3$ nanorods.

The atomic ratio of Mo to Fe in the Fe(OH)$_3$@α-MoO$_3$ core/shell nanorods is about 1.45:1. The atomic ratio of Mo to Fe in the nanorods was also determined by coupled plasma-optical emission spectroscopy (IRIS Interepid II XSP, Thermo Electron Corporation), and the value is about 1.39:1. Thus, the results above further confirm that Fe(OH)$_3$ in the Fe(OH)$_3$@α-MoO$_3$ core/shell nanostructures is amorphous.

The morphology and the structure of the Fe(OH)$_3$@α-MoO$_3$ core/shell nanostructures were investigated by SEM and TEM analyses. Figure 2a shows a SEM image of the core/shell nanostructures. It is clearly found that the average diameter of the Fe(OH)$_3$@α-MoO$_3$ core/shell nanostructures is significantly increased, in comparison with the pristine α-MoO$_3$ nanorods, but their length is decreased slightly which may result from the acid etching. TEM image (Figure 2b) shows that the Fe(OH)$_3$ shell
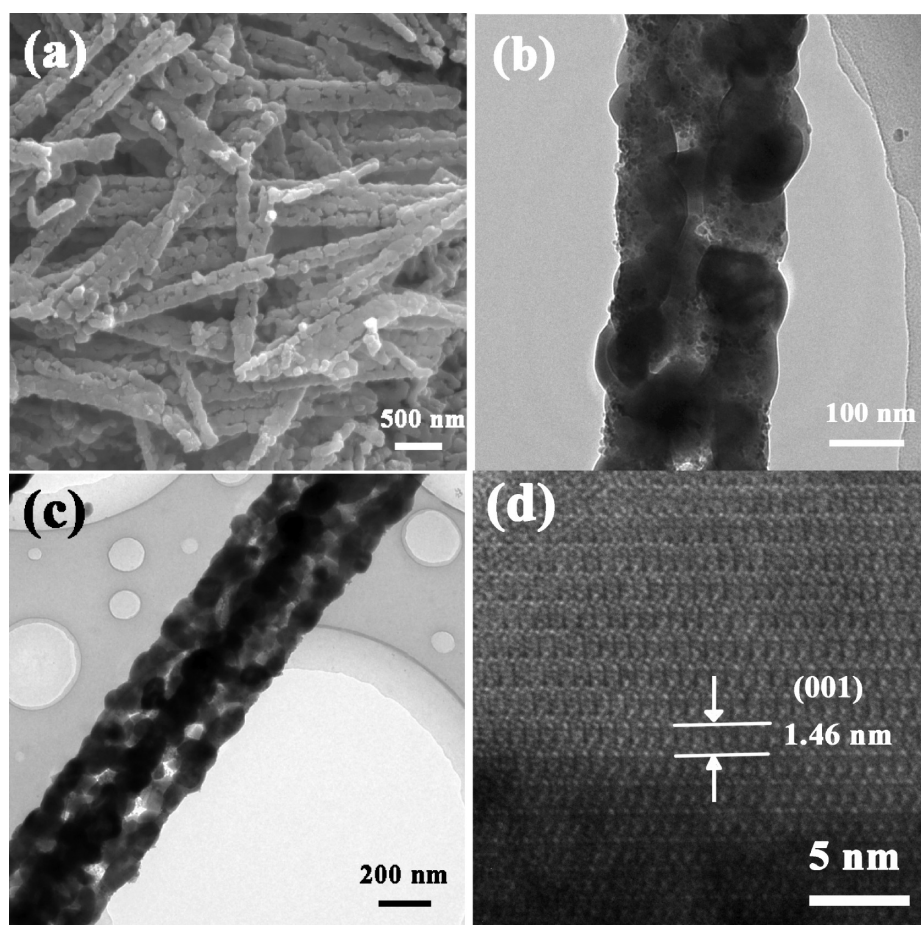
Figure 5. Structural characterization of the porous $Fe_2(MoO_4)_3$ nanorods. (a) SEM image, (b, c) TEM images, and (d) HRTEM image.

materials are composed of a thin film coated on the surface of α-MoO_3 nanorods and additional nanoplates (indicated by the black arrows) grown along the vertical direction of the thin film (between the white lines in Figure 2c). Magnified TEM image (Figure 2c) demonstrates that the width of the $Fe(OH)_3$ thin film and the length of the $Fe(OH)_3$ nanoplates are about 30 and 55 nm, respectively. Figure 2d shows that the $Fe(OH)_3$ nanostructures can be also deposited on the top of α-MoO_3 nanorods.

Figure 3 shows the EDX elemental mappings of a single $Fe(OH)_3@\alpha$-MoO_3 core/shell nanorods, in which the area of the single nanorod is marked with the white lines. It can be clearly found that the Mo element distributes mainly in the core region, whereas Fe and O elements distributes in the whole region of the nanorods, further confirming the formation of the $Fe(OH)_3@\alpha$-MoO_3 core/shell nanostructures.

**3.2. In situ Diffusion growth of Porous $Fe_2(MoO_4)_3$ Nanorods.** After the dried $Fe(OH)_3@\alpha$-MoO_3 nanorods were thermally treated at 500 °C for 4 h in air, the porous $Fe_2(MoO_4)_3$ nanorods could be obtained. Figure 4 shows a XRD pattern of the $Fe_2(MoO_4)_3$ nanorods. All diffraction peaks marked with Miller indices in the pattern can be indexed to monoclinic $Fe_2(MoO_4)_3$ (JCPDS, no. 83−1701, cell parameters: a = 15.707 Å, b = 9.231 Å, c = 18.204 Å, β = 125.25°). No significant peaks from Fe_2O_3 and α-MoO_3 were detected by the XRD measurement, suggesting that the nanorods are mainly composed of the $Fe_2(MoO_4)_3$ phase.

The morphology and the structure of the $Fe_2(MoO_4)_3$ nanorods were investigated by SEM and TEM analyses. The average diameter and the length of the $Fe_2(MoO_4)_3$ nanorods

are 200 nm and 1.2−4 μm, respectively, as shown in Figure 5a. Under the present experimental conditions, most of the $Fe_2(MoO_4)_3$ nanorods have a shape shown in Figure 5b. However, there are a small amount of the porous nanorods (around 2%) having a morphology like that shown in Figure 5c. Figure 5d shows high-resolution TEM (HRTEM) image of the porous nanorods. Clear lattice fringes are observed, suggesting the crystalline nature of the porous nanorods. The lattice spacings labeled in the figure is about 1.46 nm, corresponding to (001) crystal pane of monoclinic $Fe_2(MoO_4)_3$ phase. The EDS analysis (see Figure S2 in the Supporting Information) reveals that the atomic ratio of Mo to Fe is about 1.35:1, suggesting that the Fe content in the $Fe_2(MoO_4)_3$ nanorods is excess in comparison with stoichiometric $Fe_2(MoO_4)_3$.

Interestingly, there are micropores along the axial direction of the nanorods. The pore size is in range of 5−100 nm according to TEM observations. To verify this, we performed EDX mapping on individual $Fe_2(MoO_4)_3$ nanorods, as shown in Figure 6. It can be clearly seen that the Fe, M,o and O elements distribute in the whole nanorod region except in the location of the micropores. This not only demonstrates the conversion of the $Fe(OH)_3@\alpha$-MoO_3 core/shell nanostructures to the $Fe_2(MoO_4)_3$ nanorods, but also the formation of the micropores in the central part of the $Fe_2(MoO_4)_3$ nanorods. Figure S3 (Supporting Information) show the nitrogen adsorption−desorption isotherms and the corresponding Barrett−Joyner−Halenda (BJH) pore size distributions. The $Fe_2(MoO_4)_3$ nanorods exhibit a type IV hysteresis, indicating that the presence of micropores in the nanorods. The porous $Fe_2(MoO_4)_3$ nanorods
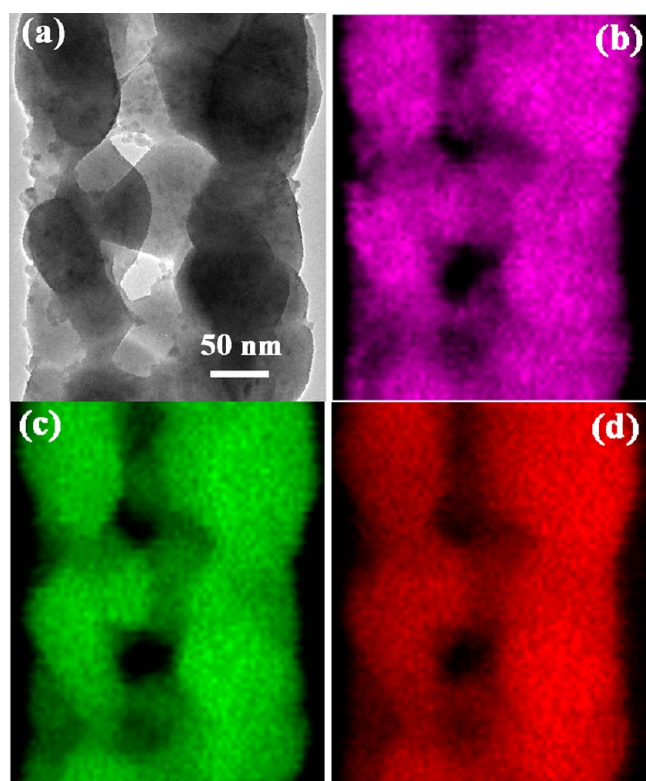
**Figure 6.** EDX elemental mappings of the porous $Fe_2(MoO_4)_3$ nanorods. (a) TEM image, and (b) Fe, (c) Mo, and (d) O elements.

Figure 7. (a) Survey XPS spectrum of the porous $Fe_2(MoO_4)_3$ nanorods, (b) Mo 3d and (c) Fe 2p spectra.

have a large Bruanuer−Emmett−Teller (BET) surface area of 24.04 m^2 g^{-1}, significantly larger than that of the pristine α-MoO_3 nanorods (8.94 m^2 g^{-1}).[54] Calculated from the desorption branch of the nitrogen isotherm with BJH method, the pore diameter in the nanorods is in the range of 4−115 nm, in good agreement with the TEM observations.
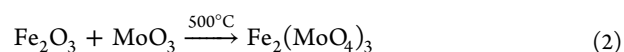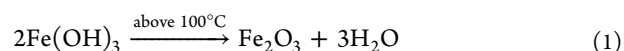
The surface electronic state and composition of the porous $Fe_2(MoO_4)_3$ nanorods were investigated by XPS analysis. The survey XPS spectrum indicates that the nanorods contain Fe, Mo, and O elements, as shown in Figure 7a. Figure 7b shows a high-resolution Mo 3d spectrum. Deconvoluted Mo 3d doublet peaks at 232.1 and 235.4 eV suggest that molybdenum is solely in the state of Mo^{6+}.[55] Figure 7c shows a high-resolution Fe 2p spectrum, in which two peaks at 711.8 and 725.6 eV corresponds to Fe $2p_{3/2}$ and Fe $2p_{1/2}$, respectively. In addition, the constant binding energies of electrons E_b (Mo $3d_{5/2}$ and Fe $2p_{3/2}$) is 479.7 eV, further confirming that Mo^{6+} as the only detected molybdenum species and Fe^{3+} as the only iron species. The surface composition with Mo/Fe = 1.4, indicating that the surface of the porous nanorods is Fe-rich with respect to stoichiometric $Fe_2(MoO_4)_3$.[17]

On the basis of the experimental results above, a plausible formation mechanism of the porous $Fe_2(MoO_4)_3$ nanorods is proposed, as illustrated in Figure 8. The $Fe(OH)_3$ shells will be gradually changed into Fe_2O_3 phases upon initially heating (at the temperature above 100 °C, step 1 in Figure 8) through the reaction process described by eq 1. When the temperature increases to 500 °C, the encapsulated α-MoO_3 nanorods diffuse outward and react with the Fe_2O_3 shells gradually upon subsequently heating (eq 2).[21] At the initial stage, relatively small void spaces in the central part of the nanorods will be formed due to the diffusion of molybdenum oxide (step 2 in Figure 8). With the increase of the reaction time at 500 °C, the
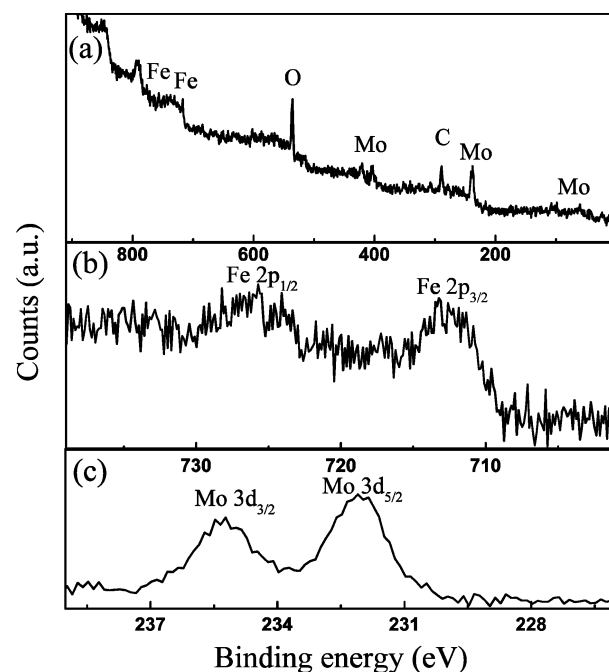
MoO_3 will totally react with Fe_2O_3, the void spaces will further extended. As a result, the uniquely porous $Fe_2(MoO_4)_3$ nanostructures are formed (step 3 in Figure 8).[21] Therefore, it is believed that the growth of the porous nanorods was achieved by an in situ diffusion process. Because of the special growth mechanism, it is relatively difficult that the porous nanorods possess a perfect single-crystal nature. Selected area electron diffraction pattern of the porous $Fe_2(MoO_4)_3$ nanorods provides an evidence for this conclusion (see Figure S4 in the Supporting Information).

$$2Fe(OH)_3 \xrightarrow{\text{above } 100°C} Fe_2O_3 + 3H_2O \qquad (1)$$

$$Fe_2O_3 + MoO_3 \xrightarrow{500°C} Fe_2(MoO_4)_3 \qquad (2)$$

3.3. H_2S Sensing Performances of Porous $Fe_2(MoO_4)_3$ Nanorods. The analyses above reveal that porous $Fe_2(MoO_4)_3$ nanorods were successfully synthesized by the in situ diffusion growth method. Considering the porous and catalytic characteristics, the $Fe_2(MoO_4)_3$ nanorods may have good gas sensing performances.[19,21] Figure 9a shows the variation of the conductance of the porous $Fe_2(MoO_4)_3$ nanorods with the increase of the temperature in air. The conductance increases with the increase of temperature demonstrates that the nanorods are of semiconductor properties. Figure 9b shows the sensor responses of the nanorods to H_2S gas with different concentrations. It can be found that the porous $Fe_2(MoO_4)_3$ nanorods have very close sensitivities to 1 ppm H_2S gas at all the tested temperatures (80−320 °C), but have significantly higher values to 5−50 ppm H_2S gases at a low temperature (80 °C) than at high temperatures (95−320 °C). Thus, the optimum working temperature of the nanorods is determined to be 80 °C. Compared to the pristine α-MoO_3 nanorods, the porous $Fe_2(MoO_4)_3$ nanorods exhibit significantly enhanced H_2S sensing properties. For example, the sensitivity of the porous $Fe_2(MoO_4)_3$ nanorods was up to 5.5 to 5 ppm H_2S at 80 °C, whereas the pristine α-MoO_3 nanorods have almost no response to 1−50 ppm H_2S at working temperatures in range of 80−180 °C, as shown in
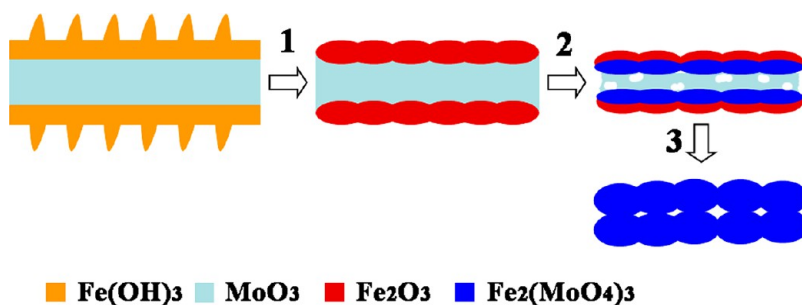
Figure 8. Illustration of the in situ diffusion growth of porous $Fe_2(MoO_4)_3$ nanorods.
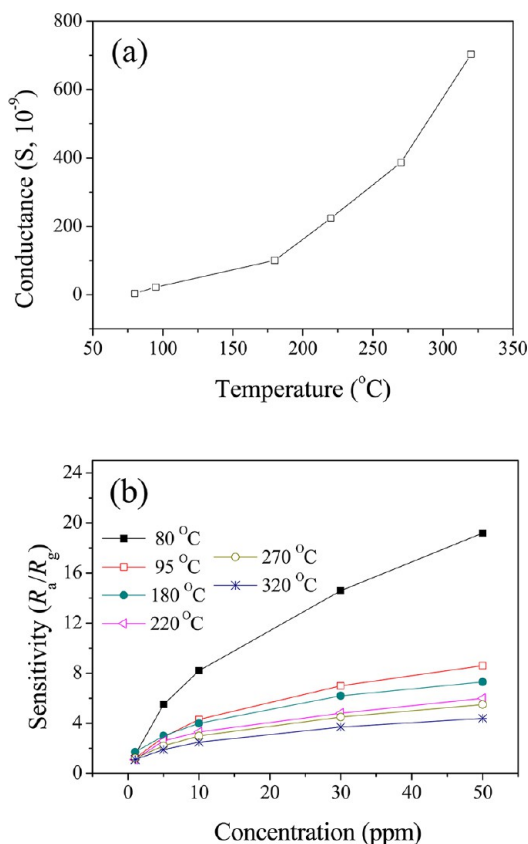
Figure 9. (a) Variation of the conductance of the porous nanorods with temperature, and (b) sensor responses of the porous $Fe_2(MoO_4)_3$ nanorods to H_2S gases with different concentrations at different working temperatures.

Figure S5 (Supporting Information). In addition, in comparison with other sensing materials such as MoO_3/ZnO cagelike nanocomposite, MoO_3/CuO p−n junctions, and CuO nanobelts, the porous $Fe_2(MoO_4)_3$ also exhibited good H_2S sensing performances.[48,54,56] For example, MoO_3/ZnO cagelike nanocomposites and CuO nanobelts had no response to 5 ppm H_2S at a working temperature of 80 °C.[54,56] Although the MoO_3/CuO p−n junctions had response to 5 ppm H_2S at 80 °C, the response did not recover after the removal of H_2S gas.[48] According to the sensing mechanism of the semiconductors,[57,58] the good H_2S sensing performance of the porous $Fe_2(MoO_4)_3$ nanorods may be related to the following factors. First, considering the micropores existed along the axial direction of the $Fe_2(MoO_4)_3$ nanorods, the actual diameter of the crystalline $Fe_2(MoO_4)_3$ nanorods is less than 80 nm, significantly smaller than the diameter of the pristine α-MoO_3 nanorods (170 nm).[21] At the same time, the surface area of the porous nanorods is significantly higher than that the

pristine α-MoO_3 nanorods (see Figure S3 in the Supporting Information). Thus the small size effect is attributed to the good sensing performances of the $Fe_2(MoO_4)_3$ nanorods. The small size effect could be also supported by the response of $Fe_2(MoO_4)_3$ nanoparticles with the average diameter of about 200 nm. The synthesis and structural characterization of the nanoparticles were shown in our previous work.[21] The $Fe_2(MoO_4)_3$ nanoparticles have very weak response to H_2S at a working temperature of 80 °C. Although the sensitivity of the nanoparticles to 50 ppm H_2S is about 1.7 at 95 °C, it is much lower than that of the porous $Fe_2(MoO_4)_3$ nanorods, as shown in Figure S5 (Supporting Information). Second, the good sensing performances of the $Fe_2(MoO_4)_3$ nanorods may be attributed to the fact that the $Fe_2(MoO_4)_3$ nanorods has many pores, which leads to the diffusion of more gas molecules into the nanorods upon their exposure to H_2S gases. In addition, as the porous nanorods exposed to H_2S gas, H_2S reacts with the oxygen adsorbates, which can be described by

$$H_2S + 3O^-(ads) \rightarrow H_2O + SO_2 + 3e^- \tag{3}$$

$$H_2S + 3O^{2-}(ads) \rightarrow H_2O + SO_2 + 6e^- \tag{4}$$
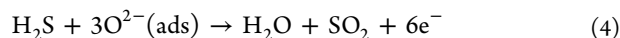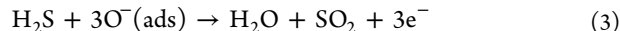
These reactions release electrons, and the released electrons will decrease the resistance of the nanorods. Thus, the nanorods have response to H_2S. It is well-known that $Fe_2(MoO_4)_3$ is an important kind of oxidation catalyst.[1−18] The catalytic ability of the $Fe_2(MoO_4)_3$ nanorods at low temperatures is beneficial to the conversion of H_2S to SO_2,[19,21] which leads to the good H_2S sensing performances of the porous nannorods.

To further investigate H_2S sensing properties of the porous $Fe_2(MoO_4)_3$ nanorods, we also measured their response to 1−50 ppm H_2S at the optimal working temperature, as shown Figure 10a. The response and recovery times were defined as the time needed for 90% of total resistance change after the sensor was exposed to the tested gas and air, respectively. As shown in Figure 10a, the response and recovery times of the porous nanorods are less than 30 and 150 s, respectively. In spite of a relatively long recovery time at a low temperature, it can be shorten sharply at higher working temperatures. For example, the recovery time is decreased to about 40 s at a working temperature of 180 °C, as shown in Figure 10b. Compared to α-MoO_3/CuO p−n junction nanorods, the porous nanorods exhibited fast recover and response time.[48]

The selectivity of the sensors is also important for their practical applications. Thus, the responses of the porous nanorods to 30 ppm acetone, ethanol, methanol, methane, H_2, ethanol, NH_3 and H_2S at 80 °C were measured. The measured results are shown in Figure S6a (Supporting Informaton). It can be observed that the porous nanorods have relatively weak response to acetone, ethanol and methanol vapors, but negligible responses
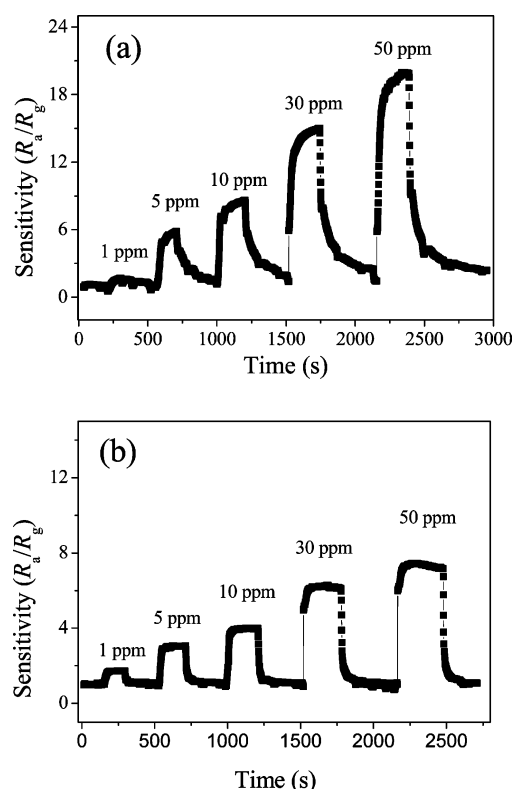
Figure 10. Time-dependent sensitivity of the porous $Fe_2(MoO_4)_3$ nanorods to H_2S gases (a) at the optimum working temperature and (b) at 180 °C.

to methane, H_2 and NH_3 gases. $S_{H2S}/S_{acetone}$, $S_{H2S}/S_{methanol}$, and $S_{H2S}/S_{ethanol}$ are 8.1, 10.4, and 13.4, respectively. Therefore, the porous nanorods have good selectivity to H_2S gas. In addition, the long-term stability of the porous nanorods exposed to 5 ppm H_2S gas indicates that the responses of the sensors are kept almost the same for 60 days of testing, as shown in Figure S6b (see the Supporting Informaton). Thus, the sensors have also good stability. The high sensitivity, fast response and recovery times, good selectivity and long-term stability allow the porous $Fe_2(MoO_4)_3$ nanorods to fabricate high-performance H_2S gas sensors.

4. CONCLUSION

In summary, we have developed an in situ diffusion method to fabricate porous $Fe_2(MoO_4)_3$ nanorods with an average diameter and a length of 200 nm and 1.2–4 μm, respectively. TEM and nitrogen adsorption–desorption measurements demonstrate that the micropores exists along the axial direction of the nanorods. The uniquely porous nanorods can be used to detect H_2S gas with a concentration down to 1 ppm at a relatively low working temperature. Moreover, the porous nanorods have very fast response and recovery times, good selectivity and long-term stability. The good H_2S sensing performances are attributed to the small size effect, porous characteristic and catalytic ability at a low temperature of the porous nanorods. In addition, the strategy presented here could be expended as a general method to synthesize other hollow/porous-type transition metal molybdate nanostructures by rational designation in nanoscale.

ASSOCIATED CONTENT

Ⓢ Supporting Information

XPS spectra of $Fe(OH)_3@\alpha$-MoO_3 core/shell nanorods, the EDS analysis, selected area electron diffraction pattern, nitrogen

adsorption–desorpton, and pore distribution of the porous $Fe_2(MoO_4)_3$ nanorods, comparison of sensing performance of the porous $Fe_2(MoO_4)_3$ nanorods with the pristine α-MoO_3 nanorods and $Fe_2(MoO_4)_3$ nanoparticles, and selectivity and stability of the porous $Fe_2(MoO_4)_3$ nanorods to H_2S. This material is available free of charge via the Internet at http://pubs.acs.org/.

AUTHOR INFORMATION

Corresponding Author

*E-mail: chenyujin@hrbeu.edu.cn (Y.-J. C.); gaopeng@hrbeu.edu.cn (P. G.); zhuchunling@hrbeu.edu.cn (C. -L. Z.).

Notes

The authors declare no competing financial interest.

REFERENCES

(1) Adkins, H.; Peterson, W. R. *J. Am. Chem. Soc.* **1931**, *53*, 1512−1520.
(2) Okamoto, Y.; Morikawa, F.; Oh-Hiraki, K.; Imanaka, T.; Teranishi, S. *J. Chem. Soc., Chem. Commun.* **1981**, 1018−1019.
(3) Machiels, C. J.; Sleight, A. W. *J. Catal.* **1982**, *76*, 238−239.
(4) Battle, P. D.; Cheetham, A. K.; LONG, G. J.; Longworth, G. *Inorg. Chem.* **1982**, *21*, 4223−4228.
(5) Jirak, Z.; R. Salmon, R.; Fournes, L.; Menil, F.; Hagenmuller, P. *Inorg. Chem.* **1982**, *21*, 4218−4223.
(6) Pernicone, N. *Catal. Today* **1991**, *11*, 85−91.
(7) Sunkou, M. R.; Mendioroz, S.; Fierro, J. L. G.; Palacios, J. M.; Guerreroruiz, A. *J. Mater. Sci.* **1995**, *30*, 496−503.
(8) Soares, A. P. V.; Portela, M. F.; Kiennemann, A.; Hilaire, L.; Millet, J. M. M. *Appl. Catal., A* **2001**, *206*, 221−229.
(9) Soares, A. P. V.; Portela, M. F.; Kiennemann, A. *Catal. Commun.* **2001**, *2*, 159−164.
(10) Bowker, M.; Holroyd, R.; Elliott, A.; Morrall, P.; Alouche, A.; Entwistle, C.; Toerncrona, A. *Catal. Lett.* **2002**, *83*, 165−176.
(11) Soares, A. P. V.; Portela, M. F.; Kiennemann, A.; Hilaire, L. *Chem. Eng. Sci.* **2003**, *58*, 1315−1322.
(12) Kim, T. H.; Ramachandra, B.; Choi, J. S.; Saidutta, M. B.; Choo, K. Y.; Song, S.-D.; Rhee, Y.-W. *Catal. Lett.* **2004**, *98*, 161−165.
(13) Soares, A. P. V.; Portela, M. F. *Catal. Rev.* **2005**, *47*, 125−174.
(14) Shirakawa, J.; Nakayama, K.; Wakihara, M.; Yoshiharu, U. *J. Phys. Chem. B* **2007**, *111*, 1424−1430.
(15) House, M. P.; Carley, A.; F. Echeverria-Valda, R.; Bowker, M. *J. Phys. Chem. C* **2008**, *112*, 4333−4341.
(16) Otsuka, K.; Wang , Y. *Appl. Catal., A* **2001**, *222*, 145−161.
(17) Xu, Q.; Jia, G. Q.; Zhang, J.; Feng, Z. C.; Li, C. *J. Phys. Chem. C* **2008**, *112*, 9387−9393.
(18) Clarlsson, P. A.; Jing, D.; Skoglundh, M. *Energy Fuels* **2012**, *26*, 1984−1987.
(19) Wang, L.; Peng, B.; Guo, X. F.; Ding, W. P.; Chen, Y. *Chem. Commun.* **2009**, *45*, 1565−1567.
(20) Polanams, J.; Ray, A. D.; Watt, R. K. *Inorg. Chem.* **2005**, *44*, 3203−3209.
(21) Chen, Y. J.; Meng, F. N.; Ma, C.; Yang, Z. W.; Zhu, C. L.; Ouyang, Q. Y.; Gao, P.; Li, J. Q.; Sun, C. W. *J. Mater. Chem.* **2012**, *22*, 12900−12906.
(22) Sun, X. M.; Li, Y. D. *Angew. Chem., Int. Ed.* **2004**, *43*, 3827−3831.

3273

dx.doi.org/10.1021/am400324g | ACS Appl. Mater. Interfaces 2013, 5, 3267−3274

(23) Jiao, F.; Bruce, P. G. *Angew. Chem., Int. Ed.* **2004**, *43*, 5958−5961.

(24) Miao, J. J.; Ren, T.; Dong, L.; Zhu, J. J.; Chen, H. Y. *Small* **2005**, *1*, 802−805.

(25) Kuang, Q.; Jiang, Z. Y.; Xie, Z. X.; Lin, S. C.; Lin, Z. W.; Xie, S. Y.; Huang, R. B.; Zheng, L. S. *J. Am. Chem. Soc.* **2005**, *127*, 11777−11784.

(26) Chen, Y. J.; Xue, X. Y.; Wang, T. H. *Nanotechnology* **2005**, *16*, 1978−1982.

(27) Lou, X. W.; Yuan, C. L.; Archer, L. A. *Adv. Mater.* **2007**, *19*, 3328−3332.

(28) Jia, C. H.; Sun, L. D.; Luo, F.; Han, X. D.; Heyderman, L. J.; Yan, C. H.; Zheng, K.; Zhang, Z.; Takano, M.; Hayashi, N.; Eltschka, M.; Kl€aui, M.; R€udiger, U.; Kasama, T.; Cervera-Gontard, L.; Dunin-Borkowski, R. E.; Tzvetkov, G.; Raabe, J. *J. Am. Chem. Soc.* **2008**, *130*, 16968−16977.

(29) Zhu, C. L.; Yu, H. L.; Zhang, Y.; Wang, T. S.; Ouyang, Q. Y.; Qi, L. H.; Chen, Y. J.; Xue, X. Y. *ACS Appl. Mater. Interfaces* **2012**, *4*, 665−671.

(30) Kuo, C. H.; Huang, M. H. *J. Am. Chem. Soc.* **2008**, *130*, 12815−12820.

(31) Yang, H. G.; Zeng, H. C. *Angew. Chem., Int. Ed.* **2004**, *43*, 5930−5933.

(32) Lou, X. W.; Wang, Y.; Yuan, C. L.; Lee, J. Y.; Archer, L. A. *Adv. Mater.* **2006**, *18*, 2325−2329.

(33) Zhang, C. F.; Wu, H. B.; Yuan, C. Z.; Guo, Z. P.; Lou, X. W. *Angew. Chem., Int. Ed.* **2012**, *51*, 9592−9595.

(34) Chen, Y. J.; Gao, P.; Wang, R. X.; Zhu, C. L.; Wang, L. J.; Cao, M. S.; Jin, H. B. *J. Phys. Chem. C* **2009**, *113*, 10061−10064.

(35) Chen, Y. J.; Xiao, G.; Wang, T. S.; Ouyang, Q. Y.; Qi, L. H.; Ma, Y.; Gao, P.; Zhu, C. L.; Cao, M. S.; Jin, H. B. *J. Phys. Chem. C* **2011**, *115*, 13603−13608.

(36) Guo, J. D.; Zavalij, P.; Whittingham, M. S. *Chem. Mater.* **1994**, *6*, 357−359.

(37) Cui, X. J.; Yu, S. H.; Li, L. L.; Biao, L.; Li, H. B.; Mo, M. S.; Liu, X. M. *Chem. Eur. J.* **2004**, *10*, 218−223.

(38) Ding, Y.; Wan, Y.; Min, Y. L.; Zhang, W.; Yu, S. H. *Inorg. Chem.* **2008**, *47*, 7813−7823.

(39) Feng, M.; Zhang, M.; Song, J. M.; Li, X. G.; Yu, S. H. *ACS Nano.* **2011**, *5*, 6726−6735.

(40) Ionescu, R.; Hoel, A.; Granqvist, C. G.; Llobet, E.; Heszler, P. *Sens. Actuators, B* **2005**, *104*, 132−139.

(41) Calestani, D.; Zha, M.; Mosca, R.; Zappettini, A.; Carotta, M. C.; Natale, V. D.; Zanotti, L. *Sens. Actuators, B* **2010**, *144*, 472−478.

(42) Chen, Y. J.; Nie, L.; Xue, X. Y.; Wang, Y. G.; Wang, T. H. *Appl. Phys. Lett.* **2006**, *88*, 083105.

(43) Kolmakov, A.; Klenov, D. O.; Lilach, Y.; Stemmer, S.; Moskovits, M. *Nano Lett.* **2005**, *5*, 667−673.

(44) Huang, F. C.; Chen, Y. Y.; Wu, T. T. *Nanotechnology* **2009**, *20*, 065501.

(45) Chen, Y. J.; Xiao, G.; Wang, T. S.; Zhang, F.; Ma, Y.; Gao, P.; Zhu, C. L.; Zhang, E. D.; Xu, Z.; Li, Q. H. *Sens. Actuators, B* **2011**, *155*, 270−277.

(46) Chen, Y. J.; Xiao, G.; Wang, T. S.; Zhang, F.; Ma, Y.; Gao, P.; Zhu, C. L.; Zhang, E. D.; Xu, Z.; Li, Q. H. *Sens. Actuators, B* **2011**, *156*, 867−874.

(47) Ouyang, Q. Y.; Li, L.; Wang, Q. S.; Zhang, Y.; Wang, T. S.; Meng, F. N.; Chen, Y. J.; Gao, P. *Sens. Actuators, B* **2012**, *169*, 17−25.

(48) Wang, T. S.; Wang, Q. S.; Zhu, C. L.; Ouyang, Q. Y.; Qi, L. H.; Li, C. Y.; Xiao, G.; Gao, P.; Chen, Y. J. *Sens. Actuators, B* **2012**, *171−172*, 256−262.

(49) Xue, X. Y.; Xing, L. L.; Chen, Y. J.; Shi, S. L.; Wang, Y. G.; Wang, T. H. *J. Phys. Chem. C* **2008**, *112*, 12157−12160.

(50) Zhang, Y.; Xiang, Q.; Xu, J. Q.; Xu, P. C.; Pan, Q. Y.; Feng, Li, F. *J. Mater. Chem.* **2009**, *19*, 4701−4706.

(51) Fang, L.; Shu, Y. Y.; Wang, A.; Zhang, T. *J. Phys. Chem. C* **2007**, *111*, 2401−2408.

(52) Liu, J. P.; Li, Y. Y.; Fan, H. J.; Zhu, Z. H.; Jiang, J.; Ding, R.; Hu, Y. Y.; Huang, X. T. *Chem. Mater.* **2010**, *22*, 212−217.

(53) Ban, C. M.; Wu, Z. C.; Gillaspie, D. T.; Chen, L.; Yan, Y. F.; Blackbum, J. L.; Dillon, A. C. *Adv. Mater.* **2010**, *22*, E145−E149.

(54) Yu, H. L.; Li, L.; Gao, X. M.; Zhang, Y.; Meng, F. N.; Wang, T. S.; Xiao, G.; Chen, Y. J.; Zhu, C. L. *Sens. Actuators, B* **2012**, *171−172*, 679−685.

(55) Okamoto, Y.; Imanaka, T.; Teranishi, S. *J. Catal.* **1981**, *85*, 3798−3805.

(56) Chen, Y. J.; Meng, F. N.; Yu, H. L.; Zhu, C. L.; Wang, T. S.; Gao, P.; Ouyang, Q. Y. *Sens. Actuators, B* **2013**, *176*, 15−21.

(57) J Scott, R. W.; Yang, S. M.; Chabanis, G.; Coombs, N.; Williams, D. E.; Ozin, G. A. *Adv. Mater.* **2001**, *13*, 1468−1472.

(58) Men, H.; Gao, P.; Zhou, B. B.; Chen, Y. J.; Zhu, C. L.; Xiao, G.; Wang, L. Q.; Zhang, M. L. *Chem. Commun.* **2010**, *46*, 7581−7583.